Shape Reconstruction in Electromagnetics

Benoît CHAIGNE

Supervisors:

Jean-Antoine DÉSIDÉRI	INRIA Sophia Antipolis, Team Opale
Claude DEDEBAN	France Télécom R&D, La Turbie
Ivar GUSTAFSSON	Chalmers University of Technology
Stéphane MOTTELET	Université de Technologie de Compiègne

Master's thesis realized from September 2005 to February 2006
at the INRIA Sophia Antipolis - 2004, routes des lucioles - BP 93
06902 Sophia Antipolis cedex - France

Acknowledgments

I would like to thank Professor Jean-Antoine DÉSIDÉRI, my supervisor at the INRIA, who was always available when I was lost in my work and who welcomed me in his team.

My thanks go to Mr Claude DEDEBAN, R&D engineer at France Télécom. His experience in electromagnetic and advice were greatly useful.

I would also like to thank Professor Ivar Gustafsson, director of the master "Engineering Mathematics" at the Chalmers University of Technology, for his support and help during my year of study in Göteborg.

And last but not least I thank the whole team Opale and the people at the INRIA for sharing their experience and their cheerful mood during the training.

Contents

Chapter 1

Thesis Environment

1.1 INRIA

The **national institute for research in computer science and control**, operating under the dual authority of the Ministry of Research and the Ministry of Industry, is dedicated to fundamental and applied research in information and communication science and technology (ICST). The Institute also plays a major role in technology transfer by fostering training through research, diffusion of scientific and technical information, development, as well as providing expert advice and participating in international programs. By playing a leading role in the scientific community in the field and being in close contact with industry, INRIA is a major participant in the development of ICST in France.

Throughout its six research units in Rocquencourt, Rennes, Sophia Antipolis, Grenoble, Nancy and Bordeaux-Lille-Saclay, INRIA has a workforce of 3,500, 2,700 of whom are scientists from INRIA's partner organizations such as CNRS (the French National Center for Scientific Research), universities and leading engineering schools. They work in 130 joint research projects. Many INRIA researchers are also professors whose approximately 950 doctoral students work on theses as part of INRIA research projects.

INRIA develops many partnerships with industry and fosters technology transfer and company foundation in the field of ICST - some sixty companies have been founded. Startups are financed in particular by INRIA-Transfert, a subsidiary of INRIA that supports four startup funds, I-Source 1 and I-Source 2 (information and communication technology), C-Source for multimedia and T-Source for telecommunications. INRIA is participating in such standardization committees as the IETF, ISO or the W3C of which INRIA was the European host from 1995 to 2002. INRIA maintains important international relations and exchanges. In Europe, INRIA is involved in ERCIM which brings together 18 European research institutes. INRIA is partner in around 40 actions selected in FP6, mainly in the IST field. INRIA also collaborates with numerous scientific and academic institutions abroad (joint laboratories such as Liapunov, LIAMA, etc., associated research teams, training and internship programs).

INRIA has an annual budget of 135 million euros, 20% of which comes from its own research contracts and development products.

The Institute's strategy closely combines scientific excellence with technology transfer. INRIA's chief goal for 2003-2007 is to achieve major scientific and technological breakthroughs in the following seven priority grand challenges:

- Designing and mastering the future network infrastructures and communication services platforms;
- Developing multimedia data and multimedia information processing;
- Guaranteeing the reliability and security of software- intensive systems;
- Coupling models and data to simulate and control complex systems;
- Combining simulation, visualization and interaction;
- Modeling living structures and mechanisms;
- Fully integrating ICST into medical technology.

Some figures:

Budgetary Resources

- State contribution: 135 M Euros WT (January 2005);
- Own resources: 1/5.

Human Resources

- 3,500 persons, including 1,800 remunerated by INRIA;
- 2,700 scientists including 950 doctoral candidates and 500 post-docs and engineers;
- 1,031 INRIA permanent positions (468 researchers, 560 engineers and technicians);
- 300 trainees.

Scientific Activities (January 2005)

- 124 project-teams and 1 development project;
- 2,600 scientific publications;
- 25 international conferences organized and co-organized by INRIA (4,360 participants including 3,200 from abroad);
- 11,500 hours of teaching.

Industrial Relations (January 2005)

- 750 active research contracts;
- 175 active patents numbered;
- 120 free software licenses (freely available on INRIA's site or by CD-Rom) and commercial software licenses;
- Around 80 companies stem from INRIA, starting with Ilog which is now listed on Nasdaq to the most recent - 12 in 2000, 4 in 2001, 3 in 2002, 7 in 2003 and 7 in 2004.

Indicators

- Active contracts bringing in revenues: over 800;
- Contracts bringing in revenues signed in 2004: over 300.

1.2 Project Team Opale

OPALE: Optimization and control, numerical algorithms and integration of complex multidisciplinary systems governed by PDE

Opale is a joint project-team with JAD (CNRS and UNSA) located in Rhône Alpes and in Sophia Antipolis. It has several objectives: analyze mathematically single or multi-disciplinary coupled systems of partial differential equations arising from physics or engineering in view of their optimization or control (geometrical optimization); construct and experiment efficient numerical approximation methods (coupling algorithms, model reduction) and optimization algorithms (gradient-based and/or evolutionary algorithms, game theory); develop software platforms for the distributed parallel computation of the related discrete systems. Application problems include multi-disciplinary optimum shape design of an aircraft wing (in collaboration with Dassault Aviation), functional optimization of a rocket system (in collaboration with CNES), and optimization of antenna systems (in collaboration with France Télécom). Opale also has a strong implication in several European networks involved in aspects of code validation.

Research themes

- Numerical algorithms for multi-disciplinary optimization of PDE systems;
- Geometrical optimization;
- Software platforms for distributed parallel computing.

International and industrial relations

- Pôle Scientifique Dassault Aviation / Université Pierre et Marie Curie (Paris VI);
- CNES (Evry);
- France Télécom (La Turbie);
- Thales (Bagneux).

Participation in several European projects :

- FLOWnet, Thematic Network (database for pre-industrial code and flow validation);
- INGENET, Thematic Network (database for genetic algorithms);
- MACSInet, Network of Excellence (MAthematics, Computing and Simulation for Industry).

Chapter 2

Introduction

A reflector is a kind of antenna among others used in telecommunications. One important related problem is to manage exactly its radiation. Indeed, there are international norms that reflectors must satisfy. For example an antenna should cover a specific geographical area and avoid others. In other words the shape of a reflector has to be optimized w.r.t. some criteria.

First, in order to understand how the shape can be optimized, we consider the so-called reconstruction problem. That is, we want to optimize a reflector so that the radiation fits a measured diagram. This is an inverse problem for which we are certain there exists a solution since the measured diagram comes from a known reflector. This inverse problem reads as a minimization problem.

However such problems involve difficult numerical matters. Here we compare two different methods for solving the optimization problem, one is analytic and the other parametric. Moreover we consider axisymmetric reflectors.

In a first part we present the direct problem. We detail how the diagram is computed from a known geometry. Then we formalize the inverse problem and define the cost functionals corresponding to each method. At last we conduct a numerical case study and provide some interpretations.

Chapter 3

Direct Problem: Computing the Electric Field

The direct problem consists in solving the equation of electromagnetics for the unknown electric field given the geometry and the incident wave. We recall from [1] a few results in electromagnetics and we use the work in [4] for the application to the axisymmetric case.

3.1 Generalities and Notations

We find in Table 3.1 and Figures 3.1 and 3.2 the geometrical notations used in the following sections. Table 3.2 presents the notations in electromagnetics.

We recall that in the Cartesian basis, $\vec{R}$, $\vec{\theta}_P$ and $\vec{\varphi}_P$ are given by

$$\vec{R} = \begin{pmatrix} \sin\theta_P \cos\varphi_P \\ \sin\theta_P \sin\varphi_P \\ \cos\theta_P \end{pmatrix}, \quad \vec{\theta}_P = \begin{pmatrix} \cos\theta_P \cos\varphi_P \\ \cos\theta_P \sin\varphi_P \\ -\sin\theta_P \end{pmatrix}, \quad \vec{\varphi}_P = \begin{pmatrix} -\sin\varphi_P \\ \cos\varphi_P \\ 0 \end{pmatrix}.$$

O	coordinates origin, source location
P	point "at infinity" (far field)
$\vec{\theta}_P$	unit vector, θ direction at P
$\vec{\varphi}_P$	unit vector, φ direction at P
S	surface of the reflector
Q	point of S
$\vec{n}$	outward-directed normal vector of S at Q
$\vec{\varphi}$	unit vector, azimuth direction at Q
$\vec{s}$	unit vector, meridian tangent of S at Q
$R\vec{R}$	vector $\vec{OP}$
$\rho\vec{\rho}$	vector $\vec{OQ}$
$r\vec{r}$	vector $\vec{QP}$

Table 3.1: Geometrical Notations

$\vec{I}$	electrical current on S at Q
$\vec{E}^i$	incident electric field
$\vec{E}^s$	scattered electric field
$\vec{H}^i$	incident magnetic field
$\vec{E}$	electric field "at infinity"
μ	magnetic permeability
ϵ	electric permittivity
$\eta = \sqrt{\mu/\epsilon}$	impedance
ω	wave pulsation
$k = \omega\sqrt{\epsilon\mu} = \frac{2\pi}{\lambda}$ (see [1])	wave number

Table 3.2: Electromagnetic Notations

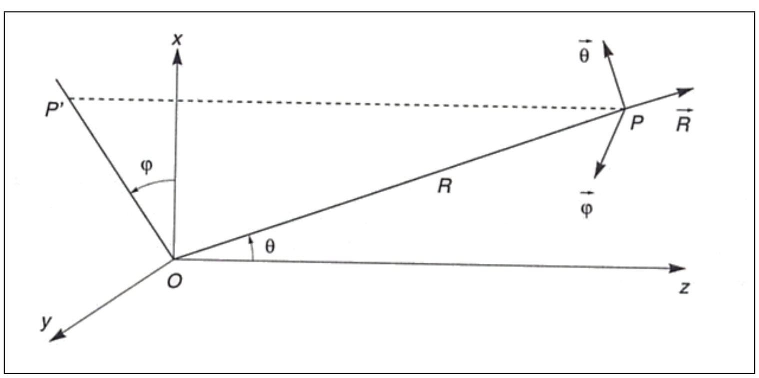

Figure 3.1: Spherical System of Coordinates

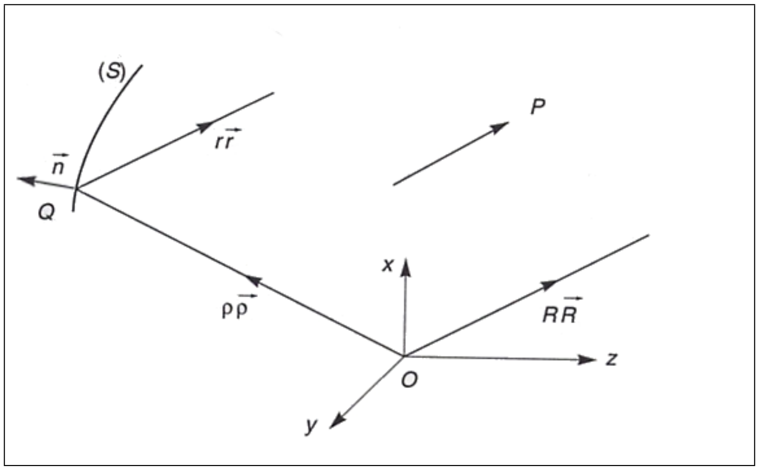

Figure 3.2: Reflector

3.2 Expressions for the Electric Field

In this section we recall the needed equations in electromagnetics, mainly taken from [1]. We consider a single source that radiates onto a reflector. Under certain assumptions we want to express the electric field. Then we define the directive gain whose representation is the aim of the direct problem.

3.2.1 Hypothesis of Physical Optics

Given a point P, we want to formulate the total electric field $\vec{E}(P)$ in spherical coordinates. The total electric field is the sum of the incident field and the scattered field by the reflector,

$$\vec{E}(P) = \vec{E^i}(P) + \vec{E^s}(P). \tag{3.1}$$

According to [1], if the diameter of the reflector is much bigger than λ, $\vec{E^s}$ is given by

$$\vec{E^s}(P) = \frac{1}{\mathrm{i}4\pi\omega\epsilon} \iint_S k^2 \vec{I} \frac{e^{-\mathrm{i}kr}}{r} + \left(\vec{I} \cdot \nabla\right) \nabla \frac{e^{-\mathrm{i}kr}}{r} dS. \tag{3.2}$$

Electromagnetic phenomena are modeled by Maxwell equations. However we chose here to approximate the current with the Physical Optics model. In this approach we consider that at each point of the surface, the reflexion is equivalent to the reflexion on the tangent plane, perfectly conductor. This means in particular that we don't model the diffraction effects du to the border of the reflector. One reason to do so is to get an explicit formula for the far field w.r.t. the geometry. Physical Optics is expressed by

$$\vec{I} = -2\vec{n} \wedge \vec{H}^i. \tag{3.3}$$

$\vec{E}^i$ and $\vec{H}^i$ are the incident electromagnetic field from the source. In our problem there are input data. We don't study the source.

Moreover, since we consider a point P *at infinity* there are terms that can be neglected (namely, terms in $\frac{1}{r^2}$, see [1]). As well, we can assume that $\vec{R}$ and $\vec{r}$ are collinear. Hence we consider that

$$\frac{1}{r} = \frac{1}{R}$$

and

$$e^{-\mathrm{i}kr} = e^{-\mathrm{i}kR} e^{\mathrm{i}k\rho(\vec{R}\cdot\vec{\rho})}.$$

Which leads to the following formula

$$\vec{E^s}(P) = -\mathrm{i}\omega\mu \frac{e^{-\mathrm{i}kR}}{4\pi R} \iint_S \left[\vec{I} - \left(\vec{I}\cdot\vec{R}\right)\vec{R}\right] e^{\mathrm{i}k\rho(\vec{R}\cdot\vec{\rho})} dS. \tag{3.4}$$

3.2.2 Scalar Expressions

One can see in (3.4) that the component of $\vec{E^s}$ in $\vec{R}$ is null. Indeed, if we project $\vec{I}$ on the spherical system at P, this yields

$$\vec{I} - \left(\vec{I}\cdot\vec{R}\right)\vec{R} = \left(\vec{I}\cdot\vec{\theta}_P\right)\vec{\theta}_P + \left(\vec{I}\cdot\vec{\varphi}_P\right)\vec{\varphi}_P. \tag{3.5}$$

From now $\vec{E^s}$ will denote the vector

$$\vec{E^s} = \frac{\mathrm{i}}{\omega\mu}\begin{bmatrix} E_\theta \\ E_\varphi \end{bmatrix} \tag{3.6}$$

where E_θ and E_φ are the transversal components. Thus (3.4) becomes

$$\vec{E^s} = \frac{e^{-\mathrm{i}kR}}{4\pi R} \iint e^{\mathrm{i}k\rho(\vec{R}\cdot\vec{\rho})} \begin{bmatrix} \vec{I}\cdot\vec{\theta}_P \\ \vec{I}\cdot\vec{\varphi}_P \end{bmatrix} dS. \tag{3.7}$$

3.2.3 Directive Gain

The directive gain is the radiation intensity, i.e. the power radiated by unit solid angle, normalized by the corresponding isotropic source [5].

In our case, the power per unit area is given by the Poynting vector

$$\mathcal{P} = \frac{1}{2}|\vec{E} \wedge \vec{H}^*| = \frac{1}{2\eta}|\vec{E}|^2. \tag{3.8}$$

So the radiation intensity U is given by $U = R^2\mathcal{P}$. We see that U depends only on θ, φ since $\vec{E}$ is a spherical wave and thus the term in R^2 disappear. Formally this reads

$$\vec{E} = \frac{e^{-\mathrm{i}kR}}{4\pi R}\vec{E}(\theta, \varphi).$$

Hence

$$U(\theta, \varphi) = \frac{1}{2\eta(4\pi)^2}|\vec{E}(\theta, \varphi)|^2. \tag{3.9}$$

Then the corresponding intensity of an isotropic source is the mean of U over all solid angles, that is

$$\begin{aligned} U_i &= \frac{1}{4\pi}\int_0^{4\pi} U(\theta, \varphi)d\Omega \\ &= \frac{1}{4\pi}\int_0^{\pi}\int_0^{2\pi} U(\theta, \varphi)\sin\theta d\theta d\varphi. \end{aligned}$$

Finally we can write the formula for the directive gain D where the constant $\frac{1}{2\eta(4\pi)^2}$ disappears

$$D(\theta, \varphi) = \frac{U(\theta, \varphi)}{U_i} = \frac{4\pi|\vec{E}(\theta, \varphi)|^2}{\int_0^{\pi}\int_0^{2\pi}|\vec{E}(\theta, \varphi)|^2\sin\theta d\theta d\varphi}. \tag{3.10}$$

Numerically this means that we need to compute by quadrature the normalization term. Alternatively, if we know the power $\mathcal{P}_a$ of the source, then $U_i = \frac{\mathcal{P}_a}{4\pi}$ and we don't need to compute the double integral. For a single source where $\vec{E^i}$ and $\vec{H^i}$ are already normed, the computed scalar $|\vec{E}(\theta, \varphi)|^2$ is the normed field, i.e., the directive gain.

3.3 Application to the Axisymmetric Case

We want now to express the surface integral as a double integral of 2 parameters under the assumption that S is axisymmetric around Oz. In other words, everything that depends on Q in (3.7) (i.e. $\vec{n}$, $\vec{H^i}$ and ρ) should be expressed as functions of these parameters.

3.3.1 Parameterization of the Surface

Let C be the curve defined by the intersection of S and the half-plane xOz for $x > 0$, in other words the meridian for $\varphi = 0$. C is a parametric curve given by

$$C \left\{ \begin{array}{l} x(s) \\ z(s) \end{array} \right. \quad s \in [0,1] \quad x, z \in \mathcal{C}^1([0,1], \mathbb{R}) \tag{3.11}$$

where $x'(s) + z'(s) \neq 0$ for all s. Because of the axisymmetry, S can be defined as a parametric surface of s and φ as follows

$$Q(s,\varphi) \in S \quad \left\{ \begin{array}{lcl} x &=& x(s)\cos\varphi \\ y &=& x(s)\sin\varphi \\ z &=& z(s) \end{array} \right. \quad s \in [0,1],\ \varphi \in [0, 2\pi]\ . \tag{3.12}$$

The vectors $\vec{\varphi}$ and $\vec{s}$

$$\vec{\varphi} = \begin{pmatrix} -\sin\varphi \\ \cos\varphi \\ 0 \end{pmatrix} \quad \vec{s} = \frac{1}{\sqrt{x'^2(s) + z'^2(s)}} \begin{pmatrix} x'(s)\cos\varphi \\ x'(s)\sin\varphi \\ z'(s) \end{pmatrix} \tag{3.13}$$

are tangent to S and orthonormal. Together with the outward-directed normal $\vec{n} = \vec{s} \wedge \vec{\varphi}$ we have an orthonormal system of coordinates at Q. We call outward side of S the one directed to the positive z.

In addition we note

$$\vec{s}_* = \sqrt{x'^2 + z'^2}\,\vec{s}. \tag{3.14}$$

3.3.2 Electric Field

We derive the electric field formula for the axisymmetric case. As modeled in (3.3) $\vec{I}$ is tangent to the surface:

$$\begin{array}{rcl} \sqrt{x'^2 + z'^2}\,\vec{I} &=& -2\sqrt{x'^2 + z'^2}\,\vec{n} \wedge \vec{H}^i \\ &=& 2\vec{H}^i \wedge (\vec{s}_* \wedge \vec{\varphi}) \\ &=& 2(\vec{H}^i \cdot \vec{\varphi})\vec{s}_* - 2(\vec{H}^i \cdot \vec{s}_*)\vec{\varphi} \\ &=& I_s(s,\varphi)\vec{s}_* + I_\varphi(s,\varphi)\vec{\varphi} \end{array}$$

with

$$\left\{ \begin{array}{lcl} I_s(s,\varphi) &=& 2(\vec{H}^i \cdot \vec{\varphi}) \\ I_\varphi(s,\varphi) &=& -2(\vec{H}^i \cdot \vec{s}_*) \end{array} \right. . \tag{3.15}$$

Injecting in (3.5), this yields

$$\begin{aligned}\sqrt{x'^2+z'^2}\left(\vec{I}-(\vec{I}\cdot\vec{R})\vec{R}\right) &= I_\varphi(s,\varphi)\left(\vec{\varphi}-(\vec{\varphi}\cdot\vec{R})\vec{R}\right)\\ &\quad +I_s(s,\varphi)\left(\vec{s}_*-(\vec{s}_*\cdot\vec{R})\vec{R}\right)\end{aligned}$$

with

$$\begin{aligned}\vec{\varphi}-(\vec{\varphi}\cdot\vec{R})\vec{R} &= (\vec{\varphi}\cdot\vec{\theta}_P)\vec{\theta}_P+(\vec{\varphi}\cdot\vec{\varphi}_P)\vec{\varphi}_P\\ &= -\cos\theta_P\sin(\varphi-\varphi_P)\vec{\theta}_P\\ &\quad +\cos(\varphi-\varphi_P)\vec{\varphi}_P\end{aligned}$$

and

$$\begin{aligned}\vec{s}_*-(\vec{s}_*\cdot\vec{R})\vec{R} &= (\vec{s}_*\cdot\vec{\theta}_P)\vec{\theta}_P+(\vec{s}_*\cdot\vec{\varphi}_P)\vec{\varphi}_P\\ &= (x'(s)\cos\theta_P\cos(\varphi-\varphi_P)-z'(s)\sin\theta_P)\,\vec{\theta}_P\\ &\quad +(x'(s)\sin(\varphi-\varphi_P))\,\vec{\varphi}_P.\end{aligned}$$

We note $\hat{\varphi}=\varphi-\varphi_P$. Hence

$$\begin{aligned}\sqrt{x'^2+z'^2}\left(\vec{I}\cdot\vec{\theta}_P\right) &= I_s(s,\varphi)(x'(s)\cos\theta_P\cos\hat{\varphi}-z'(s)\sin\theta_P)\\ &\quad -I_\varphi(s,\varphi)\cos\theta_P\sin\hat{\varphi}\\ \sqrt{x'^2+z'^2}\left(\vec{I}\cdot\vec{\varphi}_P\right) &= I_s(s,\varphi)x'(s)\sin\hat{\varphi}+I_\varphi(s,\varphi)\cos\hat{\varphi}\end{aligned}\tag{3.16}$$

Modal Decomposition

In [4] it is explained that the current can be represented as a modal decomposition where the mth mode is

$$\left\{\begin{array}{lcl} I_s(s,\varphi) &=& I_s^p(s)\cos(m\varphi)+I_s^i(s)\sin(m\varphi)\\ I_\varphi(s,\varphi) &=& I_\varphi^p(s)\cos(m\varphi)+I_\varphi^i(s)\sin(m\varphi)\end{array}\right. .\tag{3.17}$$

Each mode can be considered independently from the others. We will consider here a single mode source.

Phase Shift

We need now to express $e^{\mathrm{i}k\rho(\vec{R}\cdot\vec{\rho})}$ in terms of s and φ. Since

$$\begin{aligned}\rho(\vec{R}\cdot\vec{\rho}) &= \begin{pmatrix} x(s)\cos\varphi\\ x(s)\sin\varphi\\ z(s)\end{pmatrix}\cdot\begin{pmatrix}\sin\theta_P\cos\varphi_P\\ \sin\theta_P\sin\varphi_P\\ \cos\theta_P\end{pmatrix}\\ &= x(s)\sin\theta_P\cos\hat{\varphi}+z(s)\cos\theta_P\end{aligned}$$

so

$$e^{\mathrm{i}k\rho(\vec{R}\cdot\vec{\rho})} = e^{\mathrm{i}kx(s)\sin\theta_P\cos\hat{\varphi}} e^{\mathrm{i}kz(s)\cos\theta_P}. \tag{3.18}$$

Change of Variables

In (3.7), according to our choice of parameterization, the surface element dS can be written

$$dS = x(s)\sqrt{x'^2 + z'^2}\, d\hat{\varphi}\, ds \tag{3.19}$$

where $\hat{\varphi} \in [-\varphi_P, 2\pi - \varphi_P]$ and $s \in [0,1]$, since $\hat{\varphi} = \varphi - \varphi_P$ and $\varphi \in [0, 2\pi]$.

Integrals for Arbitrary Mode m

We provide some details on the calculation for $\vec{E^s}$ for a single mode m. To simplify formulas we note

$$\begin{aligned} \tilde{x}(s) &= kx(s)\sin\theta_P, \\ \tilde{z}(s) &= kz(s)\cos\theta_P. \end{aligned}$$

We recall that the vector $\vec{E^s} = \begin{bmatrix} \cdot \\ \cdot \end{bmatrix}$ has 2 components in $\vec{\theta}_P$ and $\vec{\varphi}_P$ respectively. We omit consciously the term $\frac{e^{-\mathrm{i}kR}}{4\pi R}$ since it doesn't play any role in the directive gain (3.2.3).

Equations (3.18) and (3.19) in (3.7) give

$$\begin{aligned} \vec{E^s} &= \iint_S e^{\mathrm{i}\tilde{z}(s)} e^{\mathrm{i}\tilde{x}(s)\cos\hat{\varphi}} \begin{bmatrix} \vec{I}\cdot\vec{\theta}_P \\ \vec{I}\cdot\vec{\varphi}_P \end{bmatrix} dS \\ &= \int_0^1 x(s) e^{\mathrm{i}\tilde{z}(s)} \int_{-\varphi_P}^{2\pi-\varphi_P} e^{\mathrm{i}\tilde{x}(s)\cos\hat{\varphi}} \begin{bmatrix} \vec{I}\cdot\vec{\theta}_P \\ \vec{I}\cdot\vec{\varphi}_P \end{bmatrix} \sqrt{x'^2+z'^2}\, d\hat{\varphi}\, ds \end{aligned}$$

Because of (3.17) the dependence in $\hat{\varphi}$ is 2π-periodic and we can integrate over any period. Together with (3.16) we have

$$\begin{aligned} \vec{E^s} = & \int_0^1 x(s) e^{\mathrm{i}\tilde{z}(s)} \int_0^{2\pi} e^{\mathrm{i}\tilde{x}(s)\cos\hat{\varphi}} \times \\ & \begin{bmatrix} A_1\cos(m\hat{\varphi})\cos\hat{\varphi} + A_2\cos(m\hat{\varphi}) + A_3\sin(m\hat{\varphi})\sin\hat{\varphi} \\ B_1\sin(m\hat{\varphi})\sin\hat{\varphi} + B_2\cos(m\hat{\varphi})\cos\hat{\varphi} \end{bmatrix} d\hat{\varphi}\, ds \end{aligned}$$

where

$$\begin{cases} A_1(s) = \left(I_s^p(s)\cos(m\varphi_P) + I_s^i(s)\sin(m\varphi_P)\right) x'(s)\cos\theta_P \\ A_2(s) = -\left(I_s^p(s)\cos(m\varphi_P) + I_s^i(s)\sin(m\varphi_P)\right) z'(s)\sin\theta_P \\ A_3(s) = \left(-I_\varphi^i(s)\cos(m\varphi_P) + I_\varphi^p(s)\sin(m\varphi_P)\right)\cos\theta_P \\ B_1(s) = \left(I_s^i(s)\cos(m\varphi_P) - I_s^p(s)\sin(m\varphi_P)\right) x'(s) \\ B_2(s) = I_\varphi^p(s)\cos(m\varphi_P) + I_\varphi^i(s)\sin(m\varphi_P) \end{cases} \tag{3.20}$$

Then we can separate variables and integrate in $\hat{\varphi}$ integrals of the form

$$\int_0^{2\pi} e^{\mathrm{i}x\cos t}\cos(mt)dt \tag{3.21a}$$

$$\int_0^{2\pi} e^{\mathrm{i}x\cos t}\cos(mt)\cos t dt \tag{3.21b}$$

$$\int_0^{2\pi} e^{\mathrm{i}x\cos t}\sin(mt)\sin t dt \tag{3.21c}$$

We note [3] that

$$\int_0^{2\pi} e^{\mathrm{i}x\cos t}\cos(mt)dt = 2\pi\mathrm{i}^m J_m(x),\ \forall m \in \mathbb{N}, \tag{3.22}$$

where J_m denotes the Bessel functions of the first kind. So (3.21a) is straightforward for all m. Moreover, when $m = 0$, (3.21b) is like (3.21a) with $m = 1$ and (3.21c) is null. Else we make use of the formulas

$$\cos(mt)\cos t = \frac{1}{2}\left(\cos[(m+1)t] + \cos[(m-1)t]\right), \tag{3.23a}$$

$$\sin(mt)\sin t = -\frac{1}{2}\left(\cos[(m+1)t] - \cos[(m-1)t]\right). \tag{3.23b}$$

In addition we recall the recursive formulas for the Bessel functions [2]

$$J_{m+1} + J_{m-1} = \frac{2m}{x}J_m \tag{3.24a}$$

$$J_{m+1} - J_{m-1} = -2\frac{dJ_m}{dx} \tag{3.24b}$$

Thus we have

$$\begin{aligned}\int_0^{2\pi} e^{\mathrm{i}x\cos t}\cos(mt)\cos t dt &= \pi \mathrm{i}^{m-1}\left(J_{m-1}(x) - J_{m+1}(x)\right) &\text{(3.25a)}\\ &= 2\pi \mathrm{i}^{m-1}\frac{dJ_m}{dx}(x)\\ \int_0^{2\pi} e^{\mathrm{i}x\cos t}\sin(mt)\sin t dt &= \pi \mathrm{i}^{m-1}\left(J_{m-1}(x) + J_{m+1}(x)\right) &\text{(3.25b)}\\ &= 2\pi \mathrm{i}^{m-1}\frac{m}{x}J_m(x)\end{aligned}$$

Putting everything together gives the expression of the scattered electric field for an axisymmetric reflector and for mode m:

$$\begin{aligned}\vec{E}^s &= 2\pi \mathrm{i}^{m-1}\int_0^1 x(s)e^{\mathrm{i}\tilde{z}(s)} \times &\text{(3.26)}\\ &\left[\begin{array}{l} A_1(s)J'_m(\tilde{x}(s)) + A_2(s)\mathrm{i}J_m(\tilde{x}(s)) + A_3(s)\frac{m}{\tilde{x}(s)}J_m(\tilde{x}(s)) \\ B_1(s)\frac{m}{\tilde{x}(s)}J_m(\tilde{x}(s)) + B_2(s)J'_m(\tilde{x}(s)) \end{array}\right] ds.\end{aligned}$$

3.3.3 A Word on Sources

$\vec{E}^i$ and $\vec{H}^i$ are considered as *black boxes*. In general we will be able to compute $\vec{H}^i(Q)$ for any point Q on the reflector and $\vec{E}^i(P)$ for any point P.

The way we obtain the current reads as follows: from (3.17) we know that for all Q and the mode m we have

$$\left\{\begin{array}{lcl} I_s(s,0) &=& I_s^p(s) \\ I_\varphi(s,0) &=& I_\varphi^p(s) \\ I_s(s,\frac{\pi}{2m}) &=& I_s^i(s) \\ I_\varphi(s,\frac{\pi}{2m}) &=& I_\varphi^i(s) \end{array}\right. \tag{3.27}$$

where $\vec{I}(s,0)$ and $\vec{I}(s,\frac{\pi}{2m})$ are deduced from (3.15).

In some special cases, analytical formulas can be derived for the sources. These cases correspond to elementary dipoles [1] [5] for which we introduce Green functions:

$$\begin{aligned}G(r) &= \frac{e^{-\mathrm{i}kr}}{4\pi r}, &\text{(3.28a)}\\ G_1(r) &= \frac{1}{r}\frac{dG(r)}{dr} = -\frac{1}{r}\left(\mathrm{i}k + \frac{1}{r}\right)G(r), &\text{(3.28b)}\\ G_2(r) &= \frac{1}{r}\frac{dG_1(r)}{dr} = -\frac{1}{r}\left(-\frac{k^2}{r} + \frac{3\mathrm{i}k}{r^2} + \frac{3}{r^3}\right)G(r). &\text{(3.28c)}\end{aligned}$$

Example for $m = 1$

In the case where the dipole is Oy-oriented the incident magnetic field reads

$$\vec{H}^i = rG_1(r) \left(-\cos\varphi\vec{\theta} + \cos\theta\sin\varphi\vec{\varphi} \right).$$

Straightforwardly the current yields

$$\boxed{\begin{array}{l} I_s^i(s) = 2z(s)G_1(r) \\ I_\varphi^p(s) = 2\left(z(s)x'(s) - x(s)z'(s)\right)G_1(r) \\ I_s^p(s) = I_\varphi^i(s) = 0. \end{array}}$$

Thus it appears that there is one single mode $m = 1$.

3.4 Numerical Computation

Knowing $I_s(s, \varphi)$ and $I_\varphi(s, \varphi)$, the electric field can be computed by a double integral quadrature. Alternatively, knowing the modal decomposition of $\vec{I}$, we have a faster method with single integral quadrature for each mode.

3.4.1 Geometry

We model here the curve C. We assume we are given a set of points $\{Q\}$ in the xOz plane. From this set we define n segments $\tau_i = [Q_i^1, Q_i^2]$ of length l_i (see Fig. 3.3 for a connex example). Furthermore we note $\Delta x_i = x_i^2 - x_i^1$ and $\Delta z_i = z_i^2 - z_i^1$.

To parameterize segment τ_i we define the derivatives x' and z', which are constants over each segment, as function of the points:

$$\left\{ \begin{array}{l} x'(s) = x_i' = \sin(\vec{z}, \vec{s}_i) = \Delta x_i / l_i \\ z'(s) = z_i' = \cos(\vec{z}, \vec{s}_i) = \Delta z_i / l_i \end{array} \right. \tag{3.29}$$

where

$$\vec{z} = \begin{pmatrix} 0 \\ 0 \\ 1 \end{pmatrix}, \quad \vec{s}_i = \begin{pmatrix} \Delta x_i / l_i \\ 0 \\ \Delta z_i / l_i \end{pmatrix}.$$

In this case note that $x'^2 + z'^2 = 1$, so $\vec{s} = \vec{s}_*$.

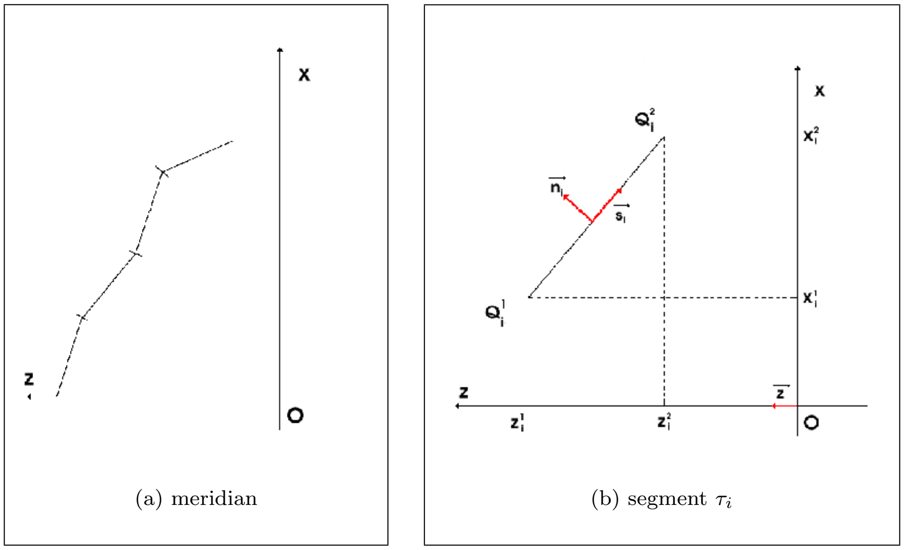

(a) meridian (b) segment τ_i

Figure 3.3: Geometry

3.4.2 Quadrature

Method

We consider a g_i-points Gaussian quadrature over τ_i for each i. We call s_i^k, $k = 1 \dots g_i$, the Gaussian curvilinear abscissae and w_i^k the corresponding weights. Moreover $x_i^k = x(s_i^k)$, $z_i^k = z(s_i^k)$, $f_i^k = f(s_i^k), \dots$. Thus the contribution of segment τ_i is

$$\vec{E_i^s} = 2\pi \mathrm{i}^{m-1} \sum_{k=1}^{g_i} w_i^k f_i^k \tag{3.30}$$

where, according to (3.26),

$$f_i^k = x_i^k e^{\mathrm{i}\tilde{z}_i^k} \left[\begin{array}{l} A_{1,i}^k J'_m(\tilde{x}_i^k) + A_{2,i}^k \mathrm{i} J_m(\tilde{x}_i^k) + A_{3,i}^k \frac{m}{\tilde{x}_i^k} J_m(\tilde{x}_i^k) \\ B_{1,i}^k \frac{m}{\tilde{x}_i^k} J_m(\tilde{x}_i^k) + B_{2,i}^k J'_m(\tilde{x}_i^k) \end{array} \right].$$

And thus over the whole reflector, we have

$$\vec{E^s} = 2\pi \mathrm{i}^{m-1} \sum_{i=1}^{n} \sum_{k=1}^{g_i} w_i^k f_i^k. \tag{3.31}$$

Implementation

We are given a set $\{P\}$ of points at infinity to compute the electric field. The full algorithm reads as follows.

Algorithm 1 Quadrature, mode m

Require: geometry (λ, $\{\tau_i\}_{i=0}^n$ $\{g_i\}_{i=1}^n$, $\{P\}$),
Require: source (mode m, $\vec{E}^i$, $\vec{H}^i$, see 3.3.2, 3.3.3)
  $k \leftarrow 2\pi/\lambda$
  for all τ_i **do**
    derivatives
    $l_i \leftarrow \sqrt{(\Delta x_i)^2 + (\Delta z_i)^2}$
    $dx_i \leftarrow \Delta x_i / l_i$, $dz_i \leftarrow \Delta z_i / l_i$
    quadrature points and weights
    x_i^k, z_i^k, w_i^k, $k = 1 \ldots g_i$
  end for
  for all P **do**
    $\vec{E}_p^s \leftarrow 0$
    compute all constants regarding P
    (precompute $\cos\theta_P$, $\sin\theta_P$, $\cos\varphi_P$, etc.)
    for all τ_i **do**
      for $k = 1$ to g_i **do**
        $\tilde{x}_i^k \leftarrow k \sin\theta_P x_i^k$
        $\tilde{z}_i^k \leftarrow k \cos\theta_P z_i^k$
        compute current $\vec{I}$ (3.27)
        compute A_1, A_2, A_3, B_1, B_2 (3.20)
        compute Bessel functions $J_m(\tilde{x}_i^k)$, $J'_m(\tilde{x}_i^k)$, $m\frac{J_m(\tilde{x}_i^k)}{\tilde{x}_i^k}$
        compute f_i^k (3.26)
        $\vec{E}_p^s \leftarrow \vec{E}_p^s + w_i^k f_i^k$
      end for
    end for
    $\vec{E}_p \leftarrow \vec{E}_p^s + \vec{E}_p^i$ *total field*
    $||\vec{E}_p||^2 \leftarrow \vec{E}_p^{\,*} \cdot \vec{E}_p$ *directive gain*
  end for

The Bessel functions are computed with the routine `rjbesl` which is to be found in the NETLIB repository (`http://www.netlib.org`) and written by W. J. Cody.

Chapter 4

Inverse Problem: Optimizing the Shape of a Reflector

In the direct problem, given a point P and a geometry in terms of $x(s)$ and $z(s)$ we can compute the scattered electric field. Inversely, considering the geometry as the unknown, how can we determine the shape of S to fit a given diagram ?

To solve this inverse problem we minimize a shape functional that penalizes the discrepancy with the given diagram. We propose two different ways to define the shape functional and we compare them on a specific case. One is analytical and the other parametric. However, once the optimization variables are defined, the strategy to reduce this cost function is the same, which is a gradient-based algorithm (see appendix A). Indeed, since the electric field is an explicit expression of the shape thanks to the Physical Optics model, we dispose of its gradient w.r.t. the shape variables x and z.

4.1 Shape Functional

For a set of points $\{P\}$, we are given a target or measured electric field noted

$$\vec{E_p^d} = \begin{pmatrix} E_p^{d,\theta} \\ E_p^{d,\varphi} \end{pmatrix}. \tag{4.1}$$

We shall then find the right shape for which the reflected field corresponds to $\vec{E_p^d}$. The idea here is to consider equation (3.26) as a functional of S. That is, for a given P we define the corresponding functional

$$\vec{E}_p[x,z] : X \times X \to \mathbb{C}^2 \tag{4.2}$$

where $X \equiv \left\{ v \in \mathcal{C}^1([0,1],\mathbb{R}) \right\}$.

Since we want to obtain the target electric field for several points $\{P\}$, it is natural to define a shape functional as a discrete L_2-norm of the difference between actual and specified electric field:

$$J(S) = J[x,z] = \sum_P \frac{1}{2} \left|\left| \vec{E}_p[x,z] - \vec{E}_p^d \right|\right|^2 \tag{4.3}$$

where the $||.||$ norm is the l_2-norm in $\mathbb{C}^2$. Thus our optimization problem reads

$$\min_{(x,z)\in X^2} J[x,z]. \tag{4.4}$$

4.1.1 Expression of the Shape Gradient

We now derive the expression of the gradient. The partial derivatives ∂_x and ∂_z represent functional derivatives.

First of all, the norm in (4.3) reads

$$\begin{aligned} \left|\left| \vec{E}_p[x,z] - \vec{E}_p^d \right|\right|^2 &= \left(E_p^\theta[x,z] - E_p^{d,\theta} \right) \overline{\left(E_p^\theta[x,z] - E_p^{d,\theta} \right)} + \\ &\quad \left(E_p^\varphi[x,z] - E_p^{d,\varphi} \right) \overline{\left(E_p^\varphi[x,z] - E_p^{d,\varphi} \right)}. \end{aligned}$$

Hence we have

$$\begin{aligned} \partial_x \left|\left| \vec{E}_p[x,z] - \vec{E}_p^d \right|\right|^2 &= \partial_x E_p^\theta[x,z] \overline{\left(E_p^\theta[x,z] - E_p^{d,\theta} \right)} \\ &\quad + \left(E_p^\theta[x,z] - E_p^{d,\theta} \right) \overline{\partial_x E_p^\theta[x,z]} \\ &\quad + \partial_x E_p^\varphi[x,z] \overline{\left(E_p^\varphi[x,z] - E_p^{d,\varphi} \right)} \\ &\quad + \left(E_p^\varphi[x,z] - E_p^{d,\varphi} \right) \overline{\partial_x E_p^\varphi[x,z]} \\ &= 2\Re \left(\overline{\partial_x E_p^\theta[x,z]} \left(E_p^\theta[x,z] - E_p^{d,\theta} \right) \right) \\ &\quad + 2\Re \left(\overline{\partial_x E_p^\varphi[x,z]} \left(E_p^\varphi[x,z] - E_p^{d,\varphi} \right) \right). \end{aligned}$$

Similarly we obtain the z derivative. Let $D\vec{E}_p$ be the Jacobian matrix

$$D\vec{E}_p = \begin{bmatrix} \partial_x E_p^\theta & \partial_z E_p^\theta \\ \partial_x E_p^\varphi & \partial_z E_p^\varphi \end{bmatrix}, \tag{4.5}$$

and D^* its conjugate transposed. Moreover we note $\vec{U_p} = \vec{E_p}[x,z] - \vec{E_p^d}$. Thus the gradient can be written

$$\nabla J = \sum_P \Re\left(D^* \vec{E_p} \cdot \vec{U_p}\right). \tag{4.6}$$

In addition note that $D\vec{E}$ reduces to $D\vec{E^s}$ since $\vec{E^i}$ does not depend on S.

4.1.2 Application to the Discrete Case

Here we consider the case where the meridian is modeled as a group of segments (cf. 3.4.1). Therefore we are looking for a shape gradient as derivatives w.r.t. the points. We recall that the set $\{Q\}$, noted also $(\mathbf{x}, \mathbf{z})$, defines n segments. Moreover we note $M = |Q|$, the cardinal of the set.

From (3.26) we can write

$$\vec{E_p^s}[x,z] = \int_0^1 \vec{F_p}(x,z,x',z')ds \tag{4.7}$$

with

$$\begin{array}{rcl} \vec{F_p}(x,z,x',z') & = & 2\pi \mathrm{i}^{m-1} x(s) e^{\mathrm{i}\tilde{z}(s)} \times \\ & & \left[\begin{array}{l} A_1(s)J'_m(\tilde{x}(s)) + A_2(s)\mathrm{i}J_m(\tilde{x}(s)) + A_3(s)\frac{m}{\tilde{x}(s)}J_m(\tilde{x}(s)) \\ B_1(s)\frac{m}{\tilde{x}(s)}J_m(\tilde{x}(s)) + B_2(s)J'_m(\tilde{x}(s)) \end{array}\right]. \end{array}$$

On segment τ_i, according to our parameterization,

$$\left\{\begin{array}{rcl} x'(\sigma) & = & \Delta x_i / l_i \\ z'(\sigma) & = & \Delta z_i / l_i \end{array}\right., \tag{4.8}$$

thus

$$\left\{\begin{array}{rcl} x(\sigma) & = & x_i^1 + \sigma \Delta x_i / l_i \\ z(\sigma) & = & z_i^1 + \sigma \Delta z_i / l_i \end{array}\right., \tag{4.9}$$

for $\sigma \in [0, l_i]$. To simplify further derivation we define the new variable $\sigma' = \sigma / l_i$, where $\sigma' \in [0,1]$ on each segment. After change of variable and injecting (4.8) and (4.9) in (4.7) the function of the points reads

$$\vec{E_p^s}(\mathbf{x}, \mathbf{z}) = \sum_{i=1}^{n} l_i \int_0^1 \vec{F_p}(Q_i^1, Q_i^2) d\sigma'. \tag{4.10}$$

Then we derivate point-wise $\vec{E_p}$ with respect to both direction, i.e., both coordinates of each point. So we define $\nabla_{\mathbf{x}}$ as

$$\nabla_{\mathbf{x}} \vec{E_p} = \left(\begin{array}{c} \nabla_{\mathbf{x}} E_p^\theta \\ \nabla_{\mathbf{x}} E_p^\varphi \end{array}\right) = \left(\begin{array}{ccc} \dots & \frac{\partial E_p^\theta}{\partial x_j} & \dots \\ \dots & \frac{\partial E_p^\varphi}{\partial x_j} & \dots \end{array}\right). \tag{4.11}$$

Similarly we define $\nabla_{\mathbf{z}}\vec{E_p}$. Note that $\nabla_{\mathbf{x}}\vec{E_p},\ \nabla_{\mathbf{z}}\vec{E_p}\ \in \mathbb{C}^{2\times M}$.

It's important to see that a point x_j can appear in two segments. In fact, the segment structure of the meridian allow us to define different non-connex parts. In this way, points at extremities of each part will appear once and the others twice (for a connex part, $n+1$ points define n segments). Therefore the derivation with respect to some x_j in $\mathbf{x}$ reads

$$\frac{\partial \vec{E_p}}{\partial x_j} = \sum_{\tau_i,\ x_j\in\tau_i} \frac{\partial l_i}{\partial x_j}\int_0^1 \vec{F_p}(Q_i^1, Q_i^2)d\sigma' + l_i\int_0^1 \frac{\partial \vec{F_p}}{\partial x_j}(Q_i^1, Q_i^2)d\sigma' \tag{4.12}$$

and similarly for $\frac{\partial \vec{E_p}}{\partial z_j}$.

According to (4.6) the shape gradient is then obtained by using (4.11) for a point-wise estimation of $D\vec{E_p}$.

$$\left\{\begin{array}{lcl} \nabla_{\mathbf{x}}J & = & \sum_P \Re\left(\nabla^*_{\mathbf{x}}\vec{E_p}\cdot\vec{U_p}\right) \\ \nabla_{\mathbf{z}}J & = & \sum_P \Re\left(\nabla^*_{\mathbf{z}}\vec{E_p}\cdot\vec{U_p}\right) \end{array}\right. , \tag{4.13}$$

where $\nabla^* \equiv \overline{\nabla^T}$. We have well $\nabla_{\mathbf{x}}J,\ \nabla_{\mathbf{z}}J\ \in \mathbb{R}^M$. Note that the first integral of the nodal derivative (4.12) is already computed with the direct problem and the second term is computed with the same quadrature rule. The only thing we need is the expression of the derivatives of $\vec{F_p}$. This is quite tedious but straightforward so we do not provide any details. We validate our formula by a Finite Difference method (see section 5.1).

4.2 Parametric Functional

In the previous method the functional depends explicitly on the geometry. In the discrete case the number of nodes needed for the precision of the computation is also the number of optimization variables. This may cause stiffness and the algorithm may fail to converge. Thus, one may want to find other optimization variables.

The method of *Free-Form Deformation* (FFD) [6] consists in the parameterization of the deformation of any solid object. In other words we use non geometrical variables with geometrical objects. The following section deals in details a 2-dimensional problem.

4.2.1 2D Free-Form Deformation

Let S^0 be an arbitrary curve in $\mathbb{R}^2$, non necessarily connex. D is a closed set of $\mathbb{R}^2$ containing S^0 that we call the deformation area. We consider an homeomorphism ϕ that maps any point of D in $[0,1] \times [0,1]$, i.e. we define a local basis for D.

$$\begin{array}{cccc} \phi & : & D & \rightarrow & [0,1] \times [0,1] \\ & & (x,z) & & (t_x, t_z) \end{array} \tag{4.14}$$

For all point (x,z) in D, *a fortiori* for all points of S^0, the deformation $(\Delta x, \Delta z)$ reads:

$$\begin{pmatrix} \Delta x \\ \Delta z \end{pmatrix} = \sum_{i=1}^{n_x} \sum_{j=1}^{n_z} b_i^x(t_x) b_j^z(t_z) \cdot \vec{p}_{ij}. \tag{4.15}$$

where n_x and n_z are called degrees of the parameterization. The $b_i^x(t)$ and $b_j^z(t)$ are basis function in $\mathcal{C}^1([0,1], \mathbb{R})$ (the deformation is smooth) and the $\vec{p}_{ij} = (p_{ij}^x \; p_{ij}^z)^\top$ are the parameters. The deformation can hence be seen as a linear combination of tensorial products of basis functions.

Bernstein polynomials (see Figure 4.1) are commonly used basis function (Bézier representation). For degree n, They are defined by

$$B_i^n(t) = \begin{pmatrix} n \\ i \end{pmatrix} t^i (1-t)^{(n-i)} \qquad i = 0 \ldots n. \tag{4.16}$$

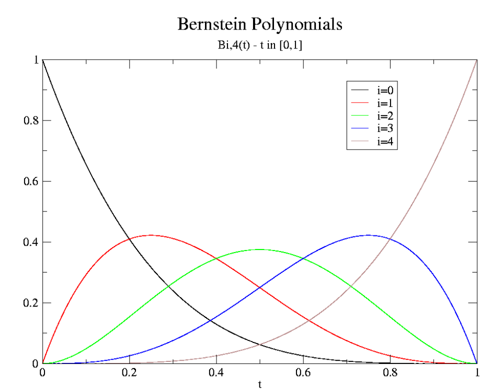

Figure 4.1: Bernstein Polynomials, n=4

For a deformation in the z-axis with $n_x = 4$ and $n_z = 0$ the deformation becomes

$$\forall t_z, \quad \Delta z = \sum_{i=1}^{4} B_i^4(t_x) p_i^z \tag{4.17}$$

In this way the geometrical deformation is simply a weighting of the functions seen on Figure 4.1. Since the deformation is smooth S does not have more singularities than S^0. This is a big difference between the first method where in the discrete case, points move independently and can create singularities.

We show a simple example of a 2D deformation on Figure (4.2).

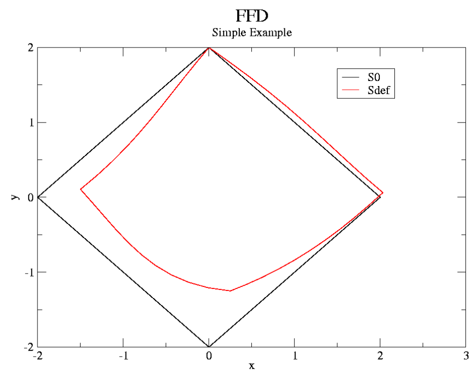

Figure 4.2: Simple 2D Example

4.2.2 Boundary Conditions

Since the parameters p do not have any direct geometrical influence, only through the basis functions, it is not easy to respect geometrical constraints. However one can see which kind of deformation the shape will be subject to while looking at certain properties of the Bernstein polynomials. In particular we focus on the boundary of D. We want to identify the right parameters for which there might be a deformation of the border.

First note that

$$\begin{array}{ll} B_0^n(0) = B_n^n(1) = 1 & \forall n \in \mathbb{N}, \\ B_i^n(0) = 0, \, \forall i > 0 & n > 0, \\ B_i^n(1) = 0, \, \forall i < n & n > 0. \end{array} \tag{4.18}$$

In example (4.17) we deduce that there can be a deformation in z for borders corresponding to $t_x = 0$ or $t_x = 1$ only with respectively p_0 or p_4 non zero.

In addition we have

$$\begin{array}{ll} B_1^{n'}(0) \neq 0, \, B_{n-1}^{n'}(1) \neq 0 & n > 0, \\ B_i^{n'}(0) = 0, \, \forall i > 1 & n > 1, \\ B_i^{n'}(1) = 0, \, \forall i < n-1 & n > 1. \end{array} \tag{4.19}$$

This give us information on the kind of deformation in the neighborhood of borders. Namely if we apply a deformation with functions B_1^n or B_{n-1}^n for $n > 1$

there will be a sharp deformation in the neighborhood. Inversely if we use the others, assuming there is no deformation of the border itself, the deformation will tend to 0 in the neighborhood.

We provide different cases where we deform a domain containing a parabola on Figure 4.3.

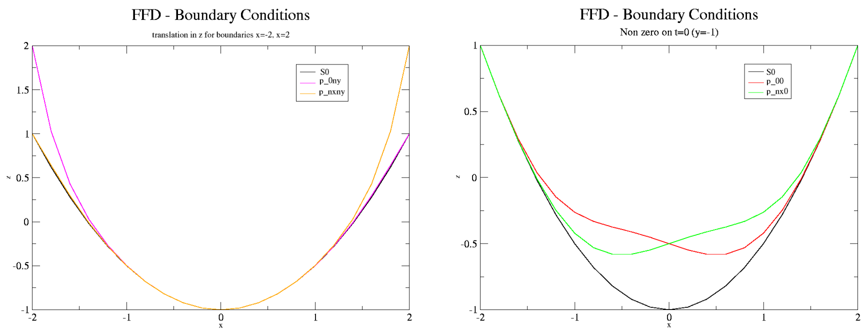

Figure 4.3: Different Boundary Conditions

4.2.3 Expression of the Parametric Functional

We apply the FFD method to our problem with Bernstein polynomials as basis functions. We define a set D which contains the initial reflector S^0 and such that the extremities belong to the border so that we can manage boundary conditions as explained in the previous section. If ΔS is a deformation of S^0 the shape reads now as a function of the parameters p

$$S(p) = S^0 + \Delta S(p) = S^0 + \sum_{i=1}^{n_x} \sum_{j=1}^{n_z} B_i^{n_x}(t_x) B_j^{n_z}(t_z) \cdot \vec{p}_{ij}. \tag{4.20}$$

Hence let $j(p)$ be the parametric functional

$$j(p) = J(S^0 + \Delta S(p)) \tag{4.21}$$

where J is given by (4.3).

4.2.4 Gradient Condensation

We express now the gradient of j w.r.t. the FFD parameters. From (4.21) and since all points of S in D are functions of p we have

$$\frac{\partial j}{\partial p_{ij}^x} = \sum_{k=1}^{M} \frac{\partial J}{\partial x_k} \frac{\partial x_k}{\partial p_{ij}^x} \tag{4.22}$$

with

$$\frac{\partial x_k}{\partial p_{ij}^x} = \frac{\partial (x_k^0 + \Delta x_k)}{\partial p_{ij}^x} = \frac{\partial \Delta x_k}{\partial p_{ij}^x} = B_i^{n_x}(t_x) B_j^{n_z}(t_z). \tag{4.23}$$

Thus the gradient is a condensation of the nodal gradient to the parameters where the distribution is determined by the value of the tensor products. This is quite natural in fact, if a parameter has more influence on a specific point, then the deviation of the functional du to the deviation of this parameter will be carried most by the corresponding point.

Chapter 5

Numerical Case Study

In this chapter we conduct experimentations. The source is an elementary dipole Oy-oriented (see section 3.3.3) located at the origin with frequency $\lambda = 10$ GHz.

5.1 Gradient Validation with FD

Description of computation for the validation of the derivative in x and z:

- Target: parabola, 51 nodes
- S^0: uniform deformation
- S for the x derivative: deviation of node 5
- S for the z derivative: deviation of node 10

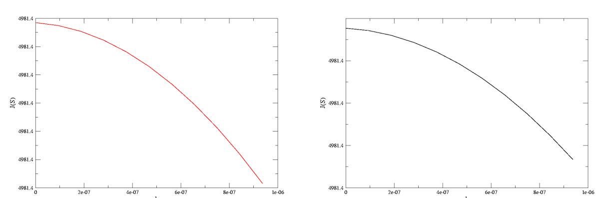

(a) w.r.t. x_{10} (b) w.r.t. z_5

Figure 5.1: Functional w.r.t. small deviations of the geometry

	AD	FD
$\partial J/\partial x_{10}$	-2208.1963	-2208.2187
$\partial J/\partial z_5$	-5989.1005	-5989.5189

Table 5.1: Analytical Derivative (AD) and Finite Difference (FD)

According to table 5.1 the derivatives are validated[1].

5.2 Analysis

Algorithm 1 has permitted us to compute the directive gain for geometries such as the ones presented in Figure 5.2. The set $\{P\}$ corresponds to two plans: $\varphi = 0$ (in red) and $\varphi = \pi/2$ (in black) for $\theta \in [0\, 2\pi]$.

On the left are the diagrams for both plans and on the right figures the meridian of the reflector.

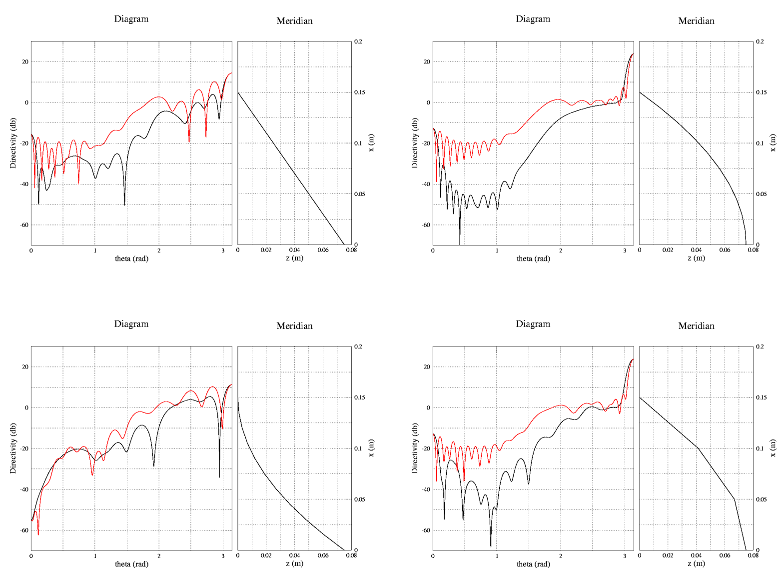

Figure 5.2: Directive Gain

[1]see appendix B for the comparison with automatic differentiation

5.3 Reconstruction

This section presents the main results in the reconstruction problem. We provide special cases which allow us to summarize the results of the numerical experimentations.

The results are presented on figures with three graphs:

- the left graph is the directive gain expressed in db where the reference value is the power of the source if there was no reflector (both plans are represented, see previous section);
- on the top right graph figures the meridian;
- on the bottom right graph figures the functional.

Moreover we adopt the following color convention:

- black if related to the initial reflector;
- brown if related to intermediate values during the optimization;
- red if related to the algorithm convergence;
- green if related to the target.

The target is a parabola discretized with 51 nodes (50 segments). We consider deformation in z ($p_{ij}^x = 0$, $\forall i, j$). Unless specified we set $n_x = 0$.

5.3.1 Small Deviation with Singularity in S^0

At first we try the methods with a quasi-uniform small perturbation of the target as initial meridian. Around node 32 can be seen a significantly non smooth part. On Figure 5.3 we observe that the algorithm has converged with nodal variables after 18 iterations. The parametric method, with $n_z = 8$, converges as well but towards a slightly worst solution (see Figure 5.4). After 39 iterations the algorithm stops. To explain this we zoom on the singular part of the meridian. This confirms what has been said in section 4.2.1: with FFD the singularities are kept. Since the target is smooth it is clear that it does not belong to the set of geometries spanned by the FFD on S^0. Whereas with the nodal variables the deformation is singular and in this case each point came back to its original position.

From now only smooth initial geometries will be considered. The reason is that practically this is very expensive to build such reflectors. So there is no need to look for singular solutions.

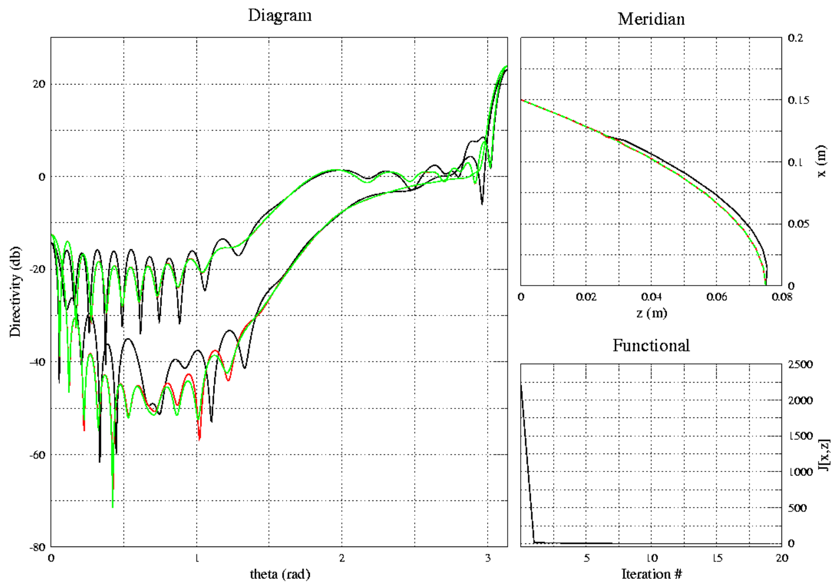

Figure 5.3: Nodal Optimization

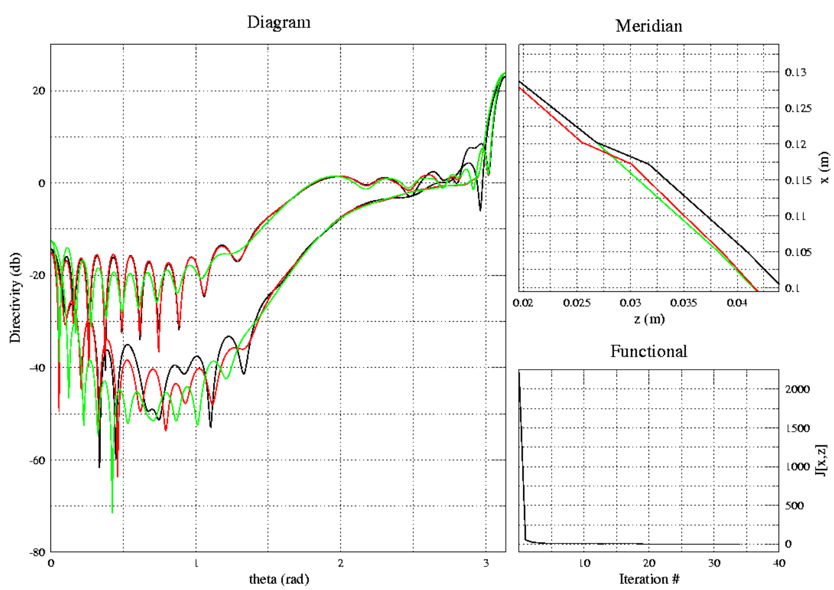

Figure 5.4: Parametric Optimization

5.3.2 Medium Deviation with Smooth S^0

Now the initial geometry is a polynomial deformation of the target such that there is no deviation at the extremities. The global deformation is much bigger than in the previous case. Consequently the initial diagram is much different from the measured one. As constraint (see section 4.2.2) we fix the first node ($x = 0$, $z = 0.075$).

One can see on Figures 5.5 and 5.6 that the algorithm converges towards completely different solutions. The one with parametric variables and with degree $n_z = 4$ is very satisfying, the target has been recovered, at the precision of the corresponding degree. On the contrary the reconstruction failed with nodal variables. Even if the diagram may fit in some area, we are not interested in non regular reflectors for the reason explained previously. In such cases the algorithm introduces too many singularities. Moreover the chosen model for the direct problem is a good approximation if the shape is regular. So the field is most probably false.

This shows that the parametric formulation can handle much larger deformation, compared to experience in 5.3.1. This comes from the fact that there are probably too many degrees of freedom with 50 optimization variables. The reduction of variables is hence necessary.

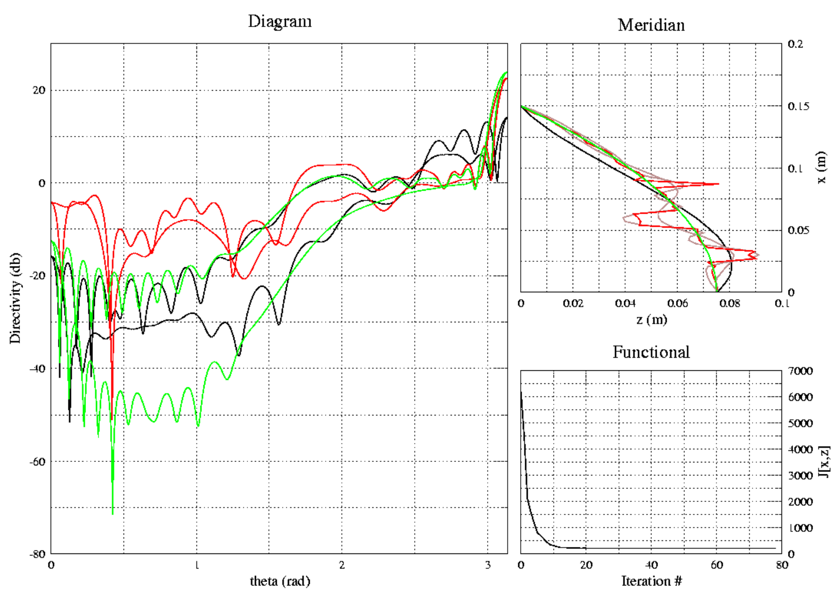

Figure 5.5: Nodal Optimization

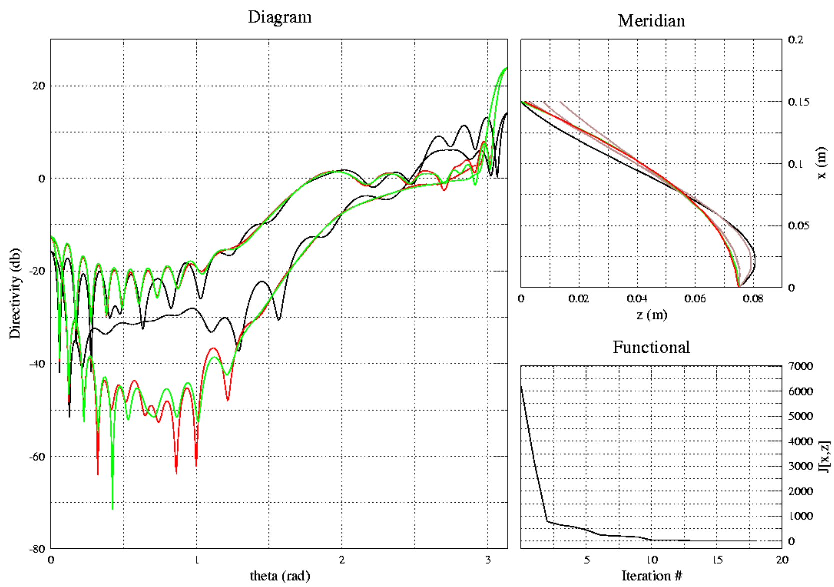

Figure 5.6: Parametric Optimization, $n = 4$

On Figure 5.7 we set the degree to $n_z = 8$ and we compare the solution with the one found with $n_z = 4$. We represent the meridian and the functional for both degrees in order to visualize the differences, especially for two areas that have been increased. It appears that the accuracy is improved while increasing the degree.

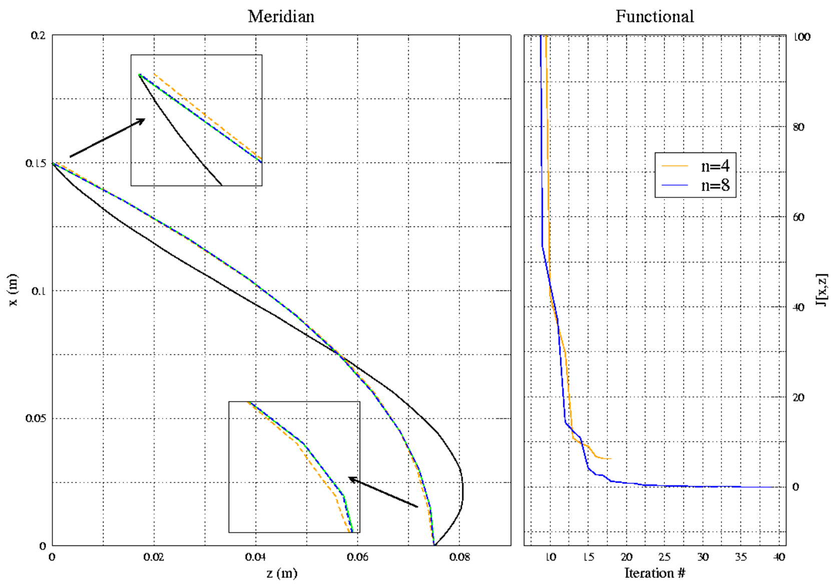

Figure 5.7: Parametric Optimization, $n = 8$

5.3.3 Large Deviation with Smooth S^0

At last we try huge deformations for S^0 to see how the algorithm behaves with the parametric variables (we do not expect any convergence with the nodal ones). We set $n_z = 4$.

Starting from a Cone

S^0 is a cone, modeled by its meridian, i.e. a straight line. We try with fixed (Figure 5.8) and free (Figure 5.9) extremities. It seems that the former case is too much constrained whereas the latter find shape similar to the target with a different focal point.

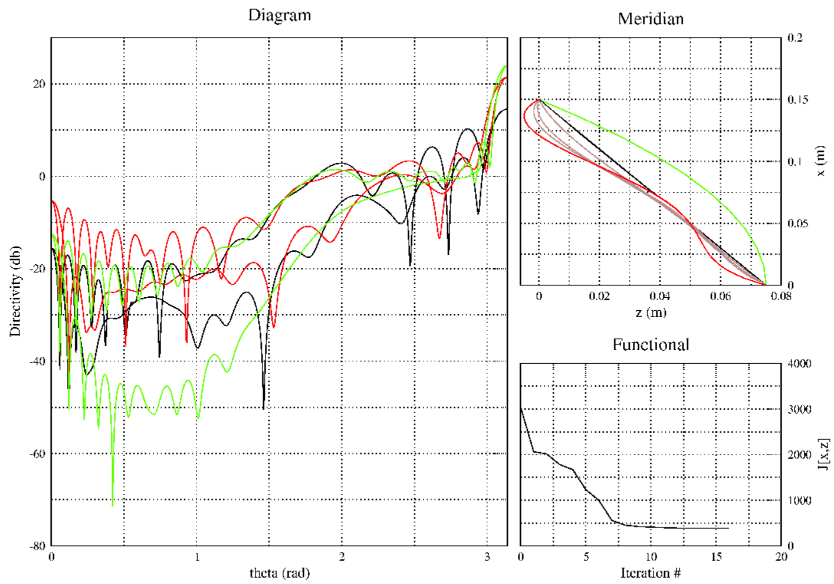

Figure 5.8: Fixed Extremities

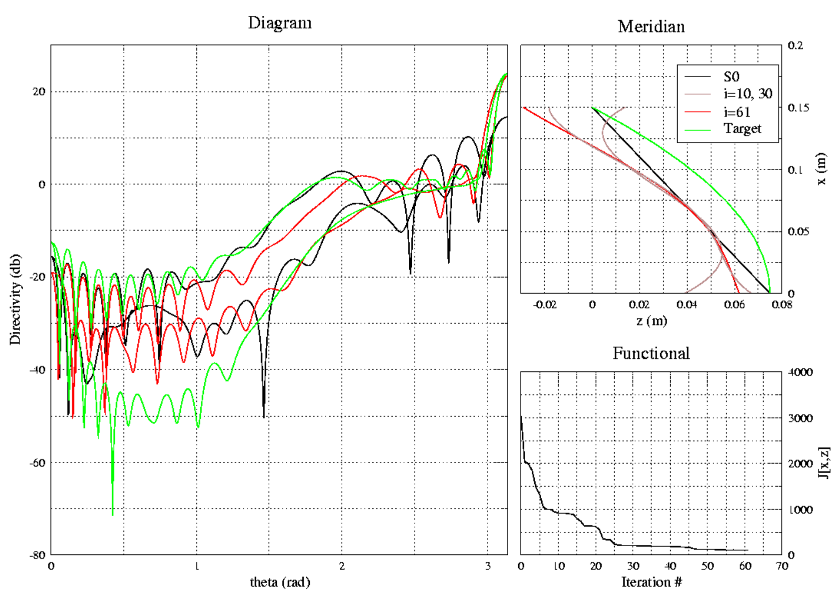

Figure 5.9: Free Extremities

Starting from a Disc

We try with another initial shape: a disc. The shape after convergence looks like the one in Figure 5.9 with another focal point.

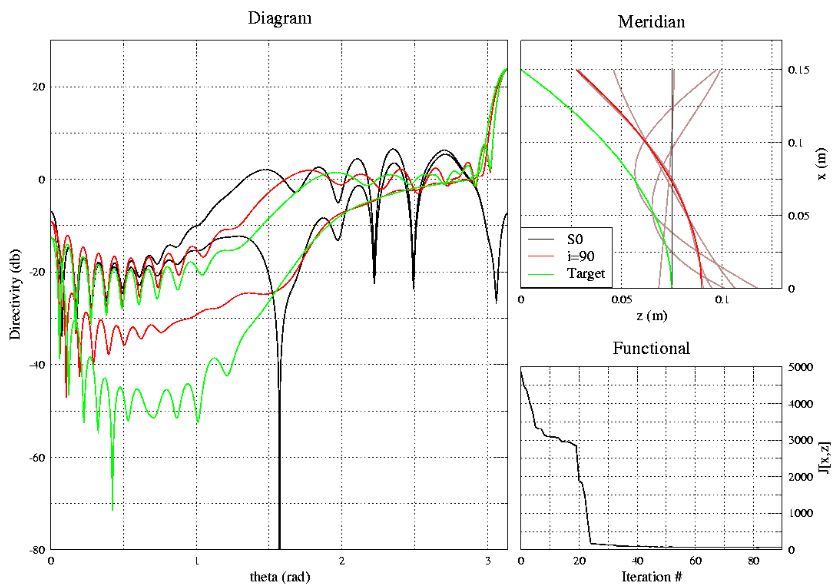

Figure 5.10: Free Extremities

Multimodal Functional

According to previous results in this section, it seems that the initial shapes are too far from the solution to recover the target shape. In general, the conducted experimentations show that convergence toward a local minimum is very likely. We show this on Figures 5.11 and 5.12. In the former we consider a single parameter problem with $n_z = 2$ and parameter p_2. The feasible geometries are shown on the right picture from the black curve to the blue one through the solution, still in green. On the left we see the functional w.r.t. the parameter p_2. Clearly this is a multimodal functional. The latter show that this configuration (probably with not enough degrees of freedom) is very sensitive to this parameter: the initial shape is chosen as far as possible from the target and such that there is convergence towards the global minima.

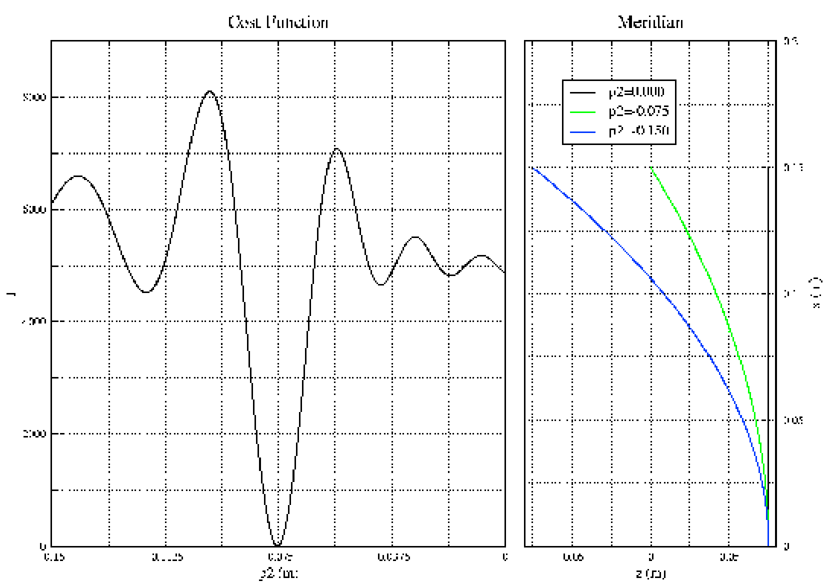

Figure 5.11: Functional w.r.t p_2

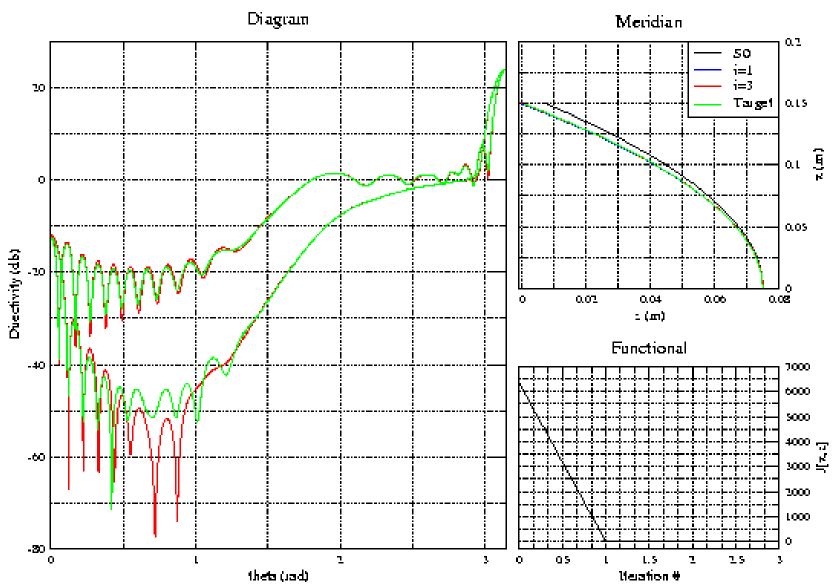

Figure 5.12: $S^0 : p_2 = -6.0 \cdot 10^{-2}$

Chapter 6

Conclusions and Perspectives

This study was intended to be a first step towards constructing an efficient numerical method for shape optimization of three-dimensional axisymmetric radiating structures incorporating and adapting various general numerical advances within the framework of the Maxwell equations.

Here we have considered the simplified approximation known as *Physical Optics* for which the electromagnetic field is known in closed form. In particular, the method yields the radiating diagram of a reflector, given the geometry (analysis code).

From this simplified analysis, we have considered the inverse problem consisting of identifying a geometry that produces a radiating diagram as close as possible to a target diagram. For this, we have used a least-squares formulation.

To make the optimization tractable, the shape deformation has been parameterized with a finite number of parameters via the so-called *Free-Form Deformation* approach. In this setting, the inverse problem reduces to a parametric optimization.

Compared with the classical "nodal formulation" of the inverse problem in which the shape gradient is discretized over the mesh used in the analysis code, the FFD approach has several merits. Both iterative convergence and control of accuracy are enhanced, by regularization and through the specification of the degree of the parameterization. Indeed, in the nodal formulation, the large number of nodes necessary to achieve sufficient accuracy makes the optimization numerically stiff, whereas the parametric optimization converges reasonably fast.

For further work, in order to improve the method, several directions will be investigated. Concerning the physical model, the *Physical Optics* approximation should be replaced by a numerical simulation of the true equations of electromagnetics (possibly preconditioned with the *Physical Optics* model). Moreover a single frequency has been considered here, so we can envisage to look for robustness w.r.t. the frequency, which is essential in practical situations. This question could be treated as a multi-point optimization. Then, concerning the numerical procedure, we can try to avoid local minima with a hybrid *evolutionary algorithm/descent algorithm* method. In addition, the convergence may be accelerated by a multi-level algorithm or the preconditioning by simplified models (such as neural networks).

Appendix A

Optimization Algorithm (from [10])

A descent direction d for the functional J at point x is such that

$$\langle d, \nabla J(x) \rangle < 0. \tag{A.1}$$

If such a direction exists this means that there is a point $\tilde{x} = x + \rho d$ for some $\rho > 0$ such that $J(\tilde{x}) < J(x)$. Thus one may find a minimum of J near x^0 with a so-called *descent method*. This is an iterative method which consists in starting from x^0 and iterate according to (A.2).

$$x^{k+1} = x^k + \rho^k d^k \tag{A.2}$$

where ρ is called the step and d^k is a direction descent for x^k. The best step is the one that minimizes $J(x^k + \rho d^k)$. However this is numerically expensive to find the optimal step since the computation of J may be expensive. The implemented algorithm is a dichotomic rule and checks that the WOLFE conditions (A.3a) and (A.3b) are satisfied

$$J(x^k + \rho^k d^k) \leq J(x^k) + \omega_1 \rho^k \left\langle \nabla J(x^k), d^k \right\rangle \tag{A.3a}$$

$$\left\langle \nabla J(x^k + \rho^k d^k), d^k \right\rangle \geq \omega_2 \left\langle \nabla J(x^k), d^k \right\rangle \tag{A.3b}$$

where $0 < \omega_1 < \omega_2 < 1$. In so doing we avoid too small steps. Practically we choose $\omega_1 = 0.05$ and $\omega_2 = 0.95$.

A natural descent direction is the opposite of the gradient itself. In this case the method is called *steepest descent*. However the convergence may be slow and inaccurate near the solution. The chosen algorithm is a Conjugate Gradient (CG) algorithm where the direction is given by

$$\begin{cases} d^0 = -\nabla J(x^0) \\ d^k = -\nabla J(x^k) + \beta d^{k-1} \end{cases}$$

where β is either the FLETCHER-REEVES coefficient

$$\beta_{FR} = \frac{||\nabla J(x^k)||^2}{||\nabla J(x^{k-1})||^2}$$

or the POLAK-RIBIÈRE coefficient

$$\beta_{PR} = \frac{\left\langle \nabla J(x^k), \nabla J(x^k) - \nabla J(x^{k-1}) \right\rangle}{||\nabla J(x^{k-1})||^2}.$$

This method is also called non-linear CG algorithm and is a generalization of the standard CG algorithm for solving symmetric positive definite systems of the form $Ax = b$. In this case the optimal step is known.

As evoked, a gradient-based algorithm is not accurate around the solution. This is du to the fact that we use only the first order Taylor expansion as information on the functional. There are better methods known as Newton methods using also the second order Taylor expansion. That is, we use not only the slope but also the curve of the functional in the neighborhood of the points at each iteration. This means that we need the Hessian of the functional J. Alternative methods estimate this Hessian at each iteration. However in our case, we could formally derive the Hessian. An other idea is to use automatic differentiation. In a first step it has been used for the first derivative of the electric field to be compared to a Finite Difference method and formal derivatives (see appendix B).

Appendix B

Automatic Differentiation

As mentioned in the previous appendix, automatic differentiation has been tested to compute the nodal derivatives of the electric field as a pilot study for a potential tool to compute the Hessian. The software TAPENADE© of the project team Tropics [7] at the INRIA Sophia-Antipolis has been used.

Here is an example of the output of the program. We compare the three methods (formal, TAPENADE and FD) for the derivative (4.12) for node 24. S is composed of 51 nodes, P is defined by $\theta = 134.0°$. `eth` and `eph` are both components of $\vec{E^s}$. The output is a complex number in the default `*` Fortran 77 format: `(real part, imaginary part)`.

```
Formal Derivative of E, id= 24
-------------------------------------------
       ===>  134. <===

deth/dx:  (9.81991174,-2.17174473)
deth/dz:  (21.9963369,-4.86068306)

deph/dx:  (-14.4643428,3.829188)
deph/dz:  (-32.3994497,8.5711727)
-------------------------------------------

TAPENADE E
-------------------------------------------
       ===>  134. <===

deth/dx:  (9.81991174,-2.17174473)
deth/dz:  (21.9963369,-4.86068306)
```

```
deph/dx:  (-14.4643428,3.829188)
deph/dz:  (-32.3994497,8.5711727)
--------------------------------------------

FD (def. in x of 1.875E-07, id= 24)
--------------------------------------------
       ===>  134. <===

Deth:  (9.81986081,-2.17187123)
Deth:  (21.9962559,-4.8610802)

Deph:  (-14.4642634,3.82937436)
Deph:  (-32.399288,8.57175076)
--------------------------------------------
```

Bibliography

[1] PAUL F. COMBES, *Micro-Ondes*, Dunod (1997) vol. 2 chapters 5, 11.2, 12.3.1, 13.4.2

[2] ERIC W. WEISSTEIN, *Bessel Function*, From MathWorld–A Wolfram Web Resource,
`http://mathworld.wolfram.com/BesselFunction.html`

[3] ERIC W. WEISSTEIN, *Bessel Function of the First Kind*, From MathWorld–A Wolfram Web Resource,
`http://mathworld.wolfram.com/BesselFunctionoftheFirstKind.html`

[4] RAYMOND BILLS, *Problème extérieur pour les equations de Maxwell Application aux antennes de révolution*, Université de Nice (1982)

[5] SOPHOCLES J. ORFANIDIS, *Electromagnetic Waves and Antennas*, Rutgers University (2004),
`http://www.ece.rutgers.edu/~orfanidi/ewa`

[6] T. SEDERBERG AND S. PARRY *Free-Form Deformation of Solid Geometric Models*, Computer Graphics (1986)

[7] TROPICS TEAM, *Tapenade v2.1, Automatic Differentiation*, INRIA Sophia Antipolis, `http://www-sop.inria.fr/tropics/`

[8] MICHEL LEVEQUE, *Conformation et optimisation des antennes à réflecteur*, stage réalisé à France Télécom R&D La Turbie (2000)

[9] JÉRÔME PICARD, *Paramétrisation hiérarchique pour l'optimisation d'un réflecteur*, stage réalisé à l'INRIA Sophia Antipolis (2004)

[10] JEAN-CHARLES GILBERT, *Optimisation différentiable : théorie et algorithmes*, INRIA Rocquencourt (2002)